Article

Dynamic cycling enhances battery lifetime

Alexis Geslin [1,2,3,4], Le Xu [2,3,4], Devi Ganapathi [1,3,4], Kevin Moy [2], William C. Chueh [1,2,3] ✉ & Simona Onori [2,3] ✉

Laboratory ageing campaigns elucidate the complex degradation behaviour of most technologies. In lithium-ion batteries, such studies aim to capture realistic ageing mechanisms to optimize cell chemistries and designs as well as to engineer reliable battery management systems. In this study, we systematically compared dynamic discharge profiles representative of electric vehicle driving to the well-accepted constant current profiles. Surprisingly, we found that dynamic discharge enhances lifetime substantially compared with constant current discharge. Specifically, for the same average current and voltage window, varying the dynamic discharge profile led to an increase of up to 38% in equivalent full cycles at end of life. Explainable machine learning revealed the importance of both low-frequency current pulses and time-induced ageing under these realistic discharge conditions. This work quantifies the importance of evaluating new battery chemistries and designs with realistic load profiles, highlighting the opportunities to revisit our understanding of ageing mechanisms at the chemistry, material and cell levels.

Lithium-ion batteries (LIBs) age through intertwined mechanisms that depend critically on conditions of use, as do solar cells, polymeric materials, biomedical devices and so on. Understanding how degradation occurs across realistic use cases is essential to accelerate material design and improve battery management systems[1]. As a well-accepted practice, the vast majority of laboratory battery studies are conducted under constant current discharge profiles[2–10]. In actual use cases, however, LIBs are subjected to dynamic current profiles during discharge[11–23].

In electric vehicles (EVs), load profiles consist of oscillations, pulses and rests[24–28]. On the one hand, several studies have investigated current profiles with alternating current frequencies, typically well above 1–10 Hz (ref. 29–38). Above such frequencies, limited degradation has been observed as electrochemical processes such as charge transfer and diffusion are only partially activated[30,39,40]. On the other hand, regenerative braking, driving in stop-and-go traffic and so on occur at lower frequencies (<1 Hz)[41], but are not well understood[42,43]. In addition, time-induced ageing (including calendar ageing at zero current[15,16,44–48]) is another critical component of realistic usage[49] but requires several years of experiments before being observed.

Therefore, a gap exists at the intersection of data-driven approaches and battery ageing experiments with realistic discharge protocols. We aimed to fill this gap by generating and analysing a non-accelerated and dynamically cycled battery dataset that represents realistic EV driving.

Thus, in this study, we compared 47 different dynamic discharge profiles with realistic average discharge currents ranging from C/16 to C/2, cycled over 24 months (where 1C corresponds to the nominal current that discharges the battery in 1 h) on 92 commercial silicon oxide–graphite/nickel cobalt aluminium lithium-ion EV energy cells. We elucidated the effect of dynamic, non-constant current discharge profiles while holding the average C-rate and voltage window constant. We found that dynamic cycling enhances battery lifetime by up to 38%. Moreover, we determined the window for the tip-over C-rate that balances time-induced ageing and cycling ageing for this commercially relevant chemistry to be approximately between 0.3C and 0.5C, in the range of realistic average C-rates. Finally, we applied explainable machine learning (ML) to deconvolute the impacts of dynamic discharge profiles on battery degradation. Specifically, we discovered the importance of low-frequency current pulses (8.2 mHz on average) in the discharge profile signal for lifetime metrics. This work illustrates

[1]Department of Materials Science and Engineering, Stanford University, Stanford, CA, USA. [2]Department of Energy Science and Engineering, Stanford University, Stanford, CA, USA. [3]Applied Energy Division, SLAC National Accelerator Laboratory, Menlo Park, CA, USA. [4]These authors contributed equally: Alexis Geslin, Le Xu, Devi Ganapathi. ✉e-mail: wchueh@stanford.edu; sonori@stanford.edu
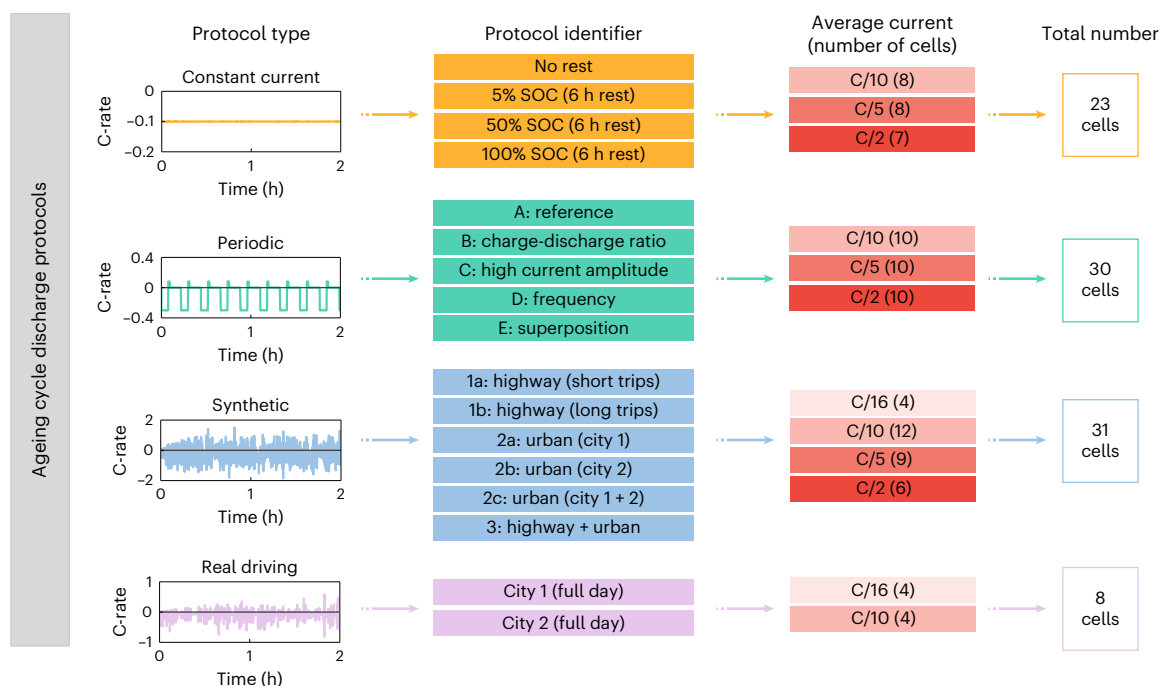
Fig. 1 | Overview of discharge protocols. Examples of the discharge data are shown for the four protocol types explored in this study. The charge protocol, voltage window and environmental chamber temperature were kept constant. For each protocol type, different variants (protocol identifier) were created. All protocols cycled the batteries from 4.2 V to 3.1 V and charged them using the same constant current–constant voltage protocol (C/2 to 4.2 V, 0.05C cut-off).

the importance of testing batteries under realistic conditions of use and challenges the broadly adopted convention of constant current discharge in the laboratory. Evaluating batteries with realistic cycling profiles is necessary to properly understand ageing mechanisms at the chemistry, material and cell levels.

Dynamic discharge profiles

We designed four different types of discharge duty cycle to simulate different operating conditions (Fig. 1). These consisted of (1) baseline constant current cycling profiles (with or without rest periods), (2) periodic duty cycles (including regenerative braking portions), (3) synthetic discharge profiles generated from field data and (4) real discharge profiles from field data. To create the synthetic profiles, we used field driving data that encompassed both highway and urban driving[41]. We tested multiple average discharge C-rates for the same protocols to simulate the effect of battery pack sizing. Based on continuous-use EV applications (autonomous and non-autonomous) such as buses, taxis, commercial or industrial vehicles, average C-rates of C/10, C/5 and C/2 were chosen as realistic driving rates, as well as C/16 (see Methods for more details). As charging protocols are typically standardized and are carried out using a constant current governed by battery management systems and charging stations[50], we used the same charging profile across all experiments (C/2 to 4.2 V, 0.05C cut-off).

We cycled all batteries in a temperature-controlled chamber set at 35 °C for technological relevance[51]. Each test protocol was duplicated. Throughout the ageing experiments, we periodically carried out reference performance tests (RPTs) and hybrid pulse power characterizations (HPPCs) to probe the state of degradation of the cells (see Methods for details). We extracted resistances from the HPPCs and fitted a half-cell differential voltage model to the C/40 RPTs to extract electrode-specific capacities (negative electrode capacity (Q_{ne}), positive electrode capacity (Q_{pe}) and lithium inventory (Q_{Li}))[52–54].

Degradation in realistic conditions

This ageing campaign provides clear evidence that dynamic cycling does not accelerate degradation, rather it enhances lifetime. Figure 2a

shows state-of-health (SOH) degradation trajectories (defined on the basis of the C/2 constant current discharge capacity obtained from the RPTs) as a function of equivalent full cycles (EFCs) for cells discharged at the same average C-rate (C/10, C/5 or C/2), either dynamically or under constant current conditions (protocol with no rest period). We observe that the constant current profiles give among the lowest cycle life across all average C-rates (with end of life (EoL) defined as 85% SOH). Supplementary Figs. 1 and 2 highlight that, from constant current to periodic profiles to synthetic and real driving profiles, the more realistic the discharge, the greater the gain in lifetime. These results confirm that constant current cycling is not representative of realistic conditions of use.

The lifetime gain due to dynamic cycling is amplified at lower average C-rates, in part because of more pronounced calendar ageing, and emphasizes the importance of carrying out ageing in dynamic and non-accelerated conditions. The low C-rates here are critical in revealing this finding, otherwise not reported in the literature[23,55]. Figure 2b shows the distributions of EFCs with respect to constant current cycling at EoL. For all C-rates (C/10, C/5 or C/2), the constant current protocols underestimate lifetime compared with almost all dynamic discharge protocols by up to 38%. For a typical powertrain, this corresponds to an underestimation of lifetime mileage of up to 195,000 miles (see Supplementary Figs. 3 and 4, Supplementary Tables 1 and 2 and Supplementary Method 1 for details of the powertrain model).

We note that, although the lower voltage cut-off is identical across all cells, the depth of discharge (DoD), defined by Coulomb counting, varies slightly from cell to cell because of differences in the overpotentials induced by the dynamic profiles. Supplementary Fig. 5 shows that such DoD variations (reaching up to 10% at C/2) have no impact on EFCs for fast-cycled cells (C/2). Although slow-cycled cells (C/10 or C/5) show a dependency on DoD, slow-cycled cells with a similar DoD (within a 4% DoD window) also exhibit spreads in EFCs in line with those of Fig. 2b,c. This confirms that the variability is mainly induced by differences in the dynamicity of the discharge profiles.

To evaluate the impact of cell-to-cell variability versus protocol-to-protocol variability, the spread between cells cycled
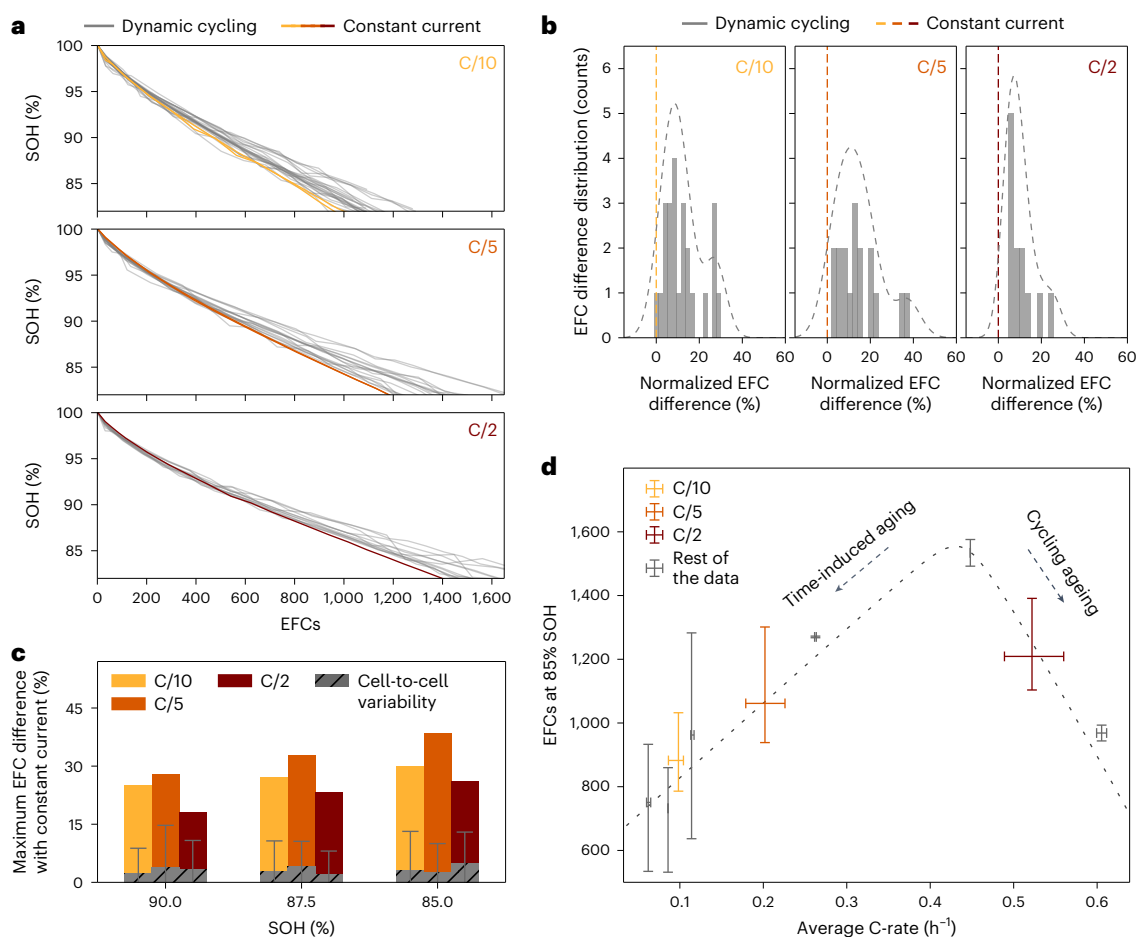
Fig. 2 | Dynamic discharge profiles lead to a wide range of degradation profiles. a, C/2 RPT discharge capacity degradation trajectories, represented by SOH, for cells cycled at C/10, C/5 and C/2. Constant current cycling profiles (in colour) underestimate battery lifetime. To compare protocols with the same average C-rates, only constant current profiles with no rest are represented here. Supplementary Fig. 1 separates each ageing protocol by colour. **b**, Distribution of EFC differences with respect to constant current cycling at 85% SOH for three different C-rates. The differences are normalized by the mean of the constant current protocols. Kernel density estimation curves, represented by the grey dashed lines, are added for visualization purposes. Supplementary Fig. 2 separates each ageing protocol by colour. **c**, Maximum EFC difference with respect to constant current cycling at 90%, 87.5% and 85% SOH for cells cycled at the same average C-rates. There are 26, 19, 13 cells in the C/10, C/5 and C/2 groups, respectively. The hatched areas show the cell-to-cell variability averaged across all protocols (there are 13, 9 and 6 protocols for the C/10, C/5 and C/2 C-rates, respectively); the whiskers represent its range. **d,** EFCs at 85% SOH as a function of the experimental average discharge C-rate. Each cross represents a group of cells cycled at a similar C-rate. The centre of the cross is the mean C-rate and mean EFC for that group of cells; the whiskers represent extrema. There are 26, 19 and 13 cells in the C/10, C/5 and C/2 groups, respectively. Cells whose average C-rate does not match C/10, C/5 or C/2 are represented in dark grey (30 cells in total).

identically was calculated for each protocol (Fig. 2c). The results show that duplicate trajectories overlay well and the average difference due to cell-to-cell variability (represented by the hatched areas) is consistently below 5%. Specifically, the range of these cell-to-cell variabilities (represented by whiskers) does not explain more than half of the variability beyond 90% SOH. This statistical analysis confirms that the protocol-to-protocol variability dominates over the cell-to-cell variability in this dataset[56]. We report on how specific attributes of the dynamic discharge protocol control lifetime metrics in a later section.

Furthermore, the spread in degradation trajectories is also observed in the low-rate C/40 capacity, the electrode-specific metrics Q_{ne}, Q_{pe} and Q_{Li}, and the discharge resistances, all extracted from the diagnostic cycles (Supplementary Fig. 6). Interestingly, the normalized low-rate capacity from the C/40 RPTs degrades at the same pace, if not faster, than the high-rate capacity (from the C/2 RPTs, Fig. 2a). This suggests that the degradation modes impacting the non-kinetic properties of the batteries (such as the loss of active material) become visible earlier than those impacting the kinetic properties of the battery

(for example, resistance growth). However, we still observed notable differences in resistance growth. Specifically, among the synthetic protocols, those derived from urban driving (protocols 2b and 2c in Fig. 1) consistently resulted in higher resistance growth across different average C-rates compared with highway-based protocols (protocols 1a and 1b; Supplementary Fig. 7).

Finally, under real-use discharge conditions, we found that there is an optimal C-rate window balancing time-induced ageing and cycling ageing (Fig. 2d). This optimal window is in the range of realistic EV discharge rates, between 0.3C and 0.5C. Up to the tipping point, the number of EFCs increases with current. Notably, while correlated with the experimental time, the C-rate is also convoluted with the DoD, as discussed earlier. Both dependencies are responsible for the trend observed here below the tipping point. Above the tipping point, cycling ageing dominates. The fact that cycling- and time-induced degradations are equally important at rates near 0.4C for our EV cells challenges conventional battery wisdom and is key for battery pack sizing and lifetime optimization. We note that this optimal operating C-rate window may depend on cell design, chemistry and ageing conditions
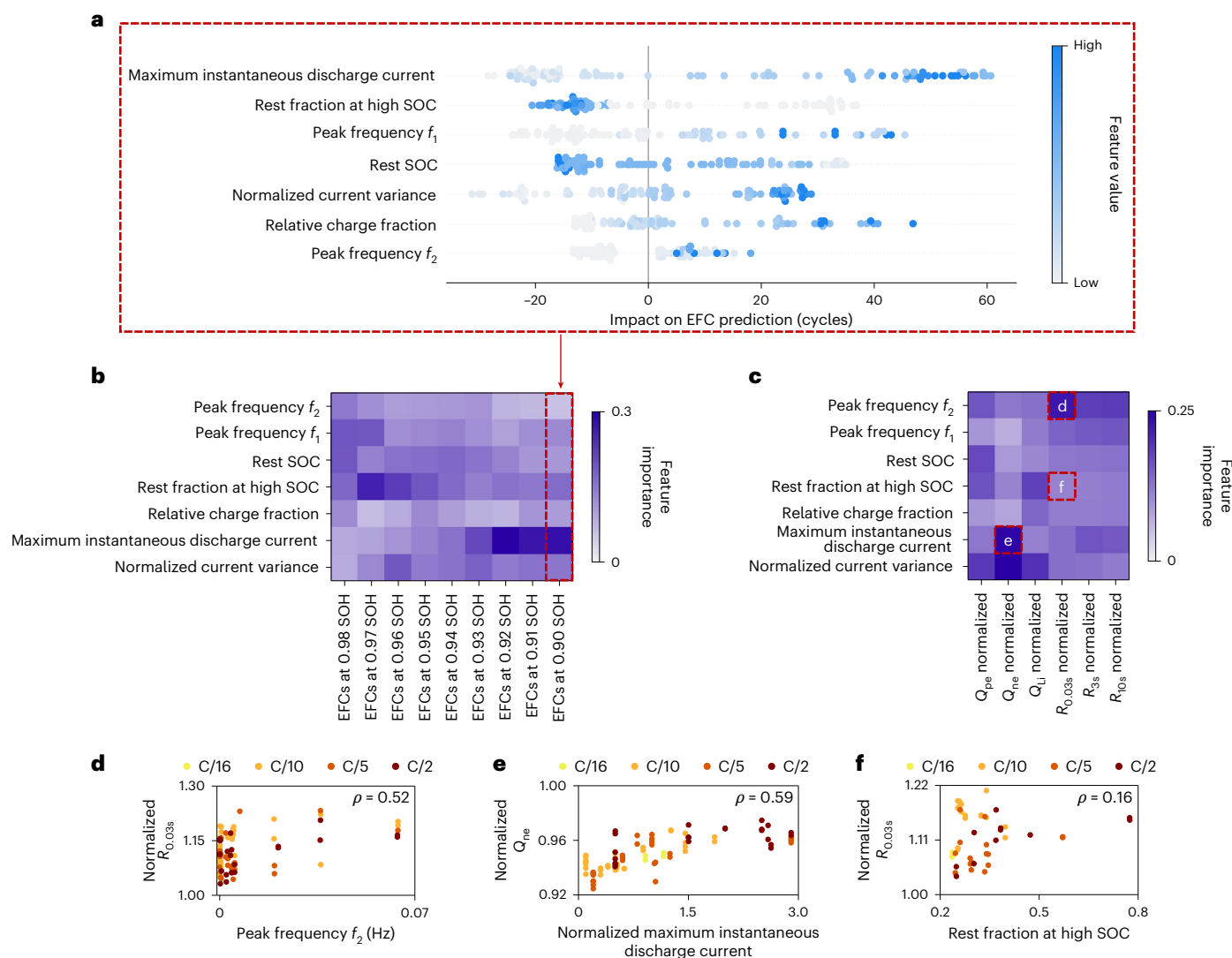
Fig. 3 | Using SHAP analysis to determine the importance of discharge profile characteristics to predict EoL metrics. SHAP analysis was used to determine the importance of various characteristics of the discharge profile to predict cycle life. As we were interested in the variability beyond the average C-rate, the average current importance is not shown. **a**, Impact of key features on predicting the EFC at 90% SOH. Each data point corresponds to a cell. **b**, Evolution of the importance of features for predicting EFCs as the cells age. **c**, Other EoL metrics at 90% SOH exhibit a more complex dependence on the discharge profile features. The raw values of each block **d**–**f** are plotted in the corresponding panels. **d**–**f**, Strong features identified by SHAP (**d**,**e**) are often correlated (for example, the Pearson coefficient ρ is reported for C/2 cells), while irrelevant features identified by SHAP analysis show weak correlation (**f**).

(such as temperature or voltage window), emphasizing the need for experiments representative of field conditions.

Impact of dynamic discharge features

To explain the variability in EoL metrics beyond the C-rate dependence illustrated in Fig. 2d, we determined the correlations between the characteristics of these discharge profiles and the degradation metrics using ML models coupled with SHapley Additive exPlanations (SHAP) analysis. Leveraging the diversity of the dynamic cycling profiles, we extracted discharge profile features such as the current variance and maximum, the relative charge (or regenerative braking) fraction and the peak frequencies from a Fourier transform of the discharge current profile (see Supplementary Table 3 for a complete list of features). Figure 3 illustrates the relative importance of the extracted characteristics for predicting EFCs (Fig. 3a,b) and EoL metrics (Fig. 3c). We confirmed the correlations identified by the SHAP analysis by plotting the duty cycle features versus the metric of interest (Fig. 3d–f).

The peak frequencies extracted from the Fourier transform of the discharge current signal are correlated with EoL metrics, in

particular with the positive electrode capacity and the resistance growth (Supplementary Fig. 8). Figure 3c shows that the Ohmic resistance, charge-transfer resistance and polarization resistance are all dominated by a key peak frequency of the dynamic discharge current profile (referred to as f_2, its distribution across all cells is illustrated in Supplementary Fig. 9), as well as the maximum instantaneous discharge current. These discharge current frequencies are all well below 1 Hz (ranging from 0.05 mHz to 64 mHz), corresponding to lithium intercalation. We hypothesize that these correlations may be due to differences in electrode particle activation at higher frequencies[57–59] and reduced local stresses and heterogeneities at low frequencies[60,61].

In addition, the electrode-specific capacities, obtained using a half-cell differential voltage model (see Methods for details), display distinct correlations with dynamic discharge features. First, the negative electrode degradation is dictated by the maximum instantaneous discharge current (which can reach up to 1,800% of the average C-rate in synthetic and real driving protocols) and the current variance. Second, the positive electrode degradation is highly convoluted, with
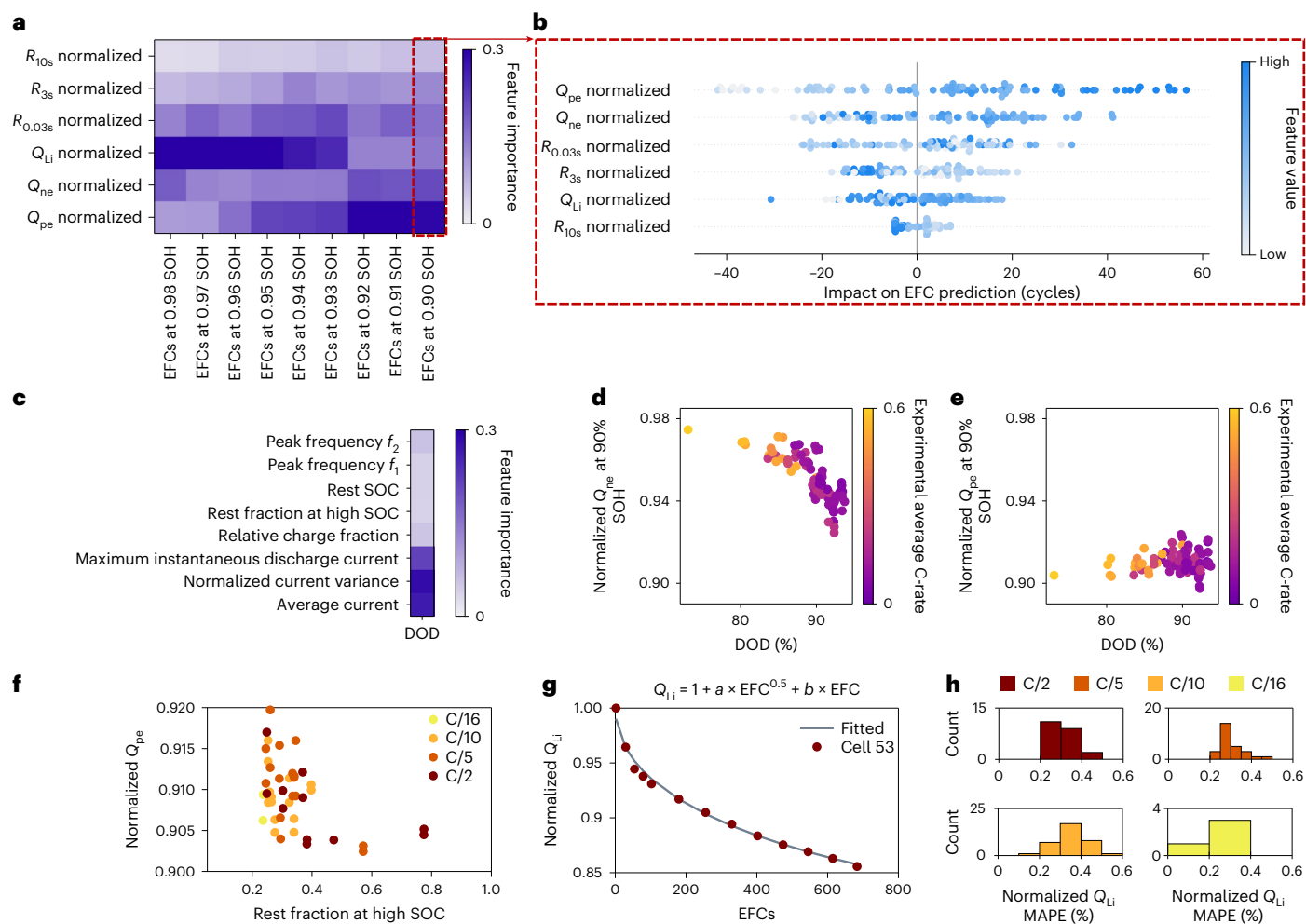
Fig. 4 | Impact and origins of degradation modes Q_{ne}, Q_{pe} and Q_{Li}. a, Impact of key degradation modes on predicting the EFCs for various SOH. **b**, At 90% SOH, multiple degradation mechanisms contribute to battery cycle life. Each data point corresponds to a cell. **c**, Impact of cycling conditions on DoD. While the voltage window is controlled, differences in overpotential will trigger the lower cut-off voltage at different DoDs. **d,e**, Negative and positive electrode capacities versus DoD for all cells. Beyond 85% DoD, the negative electrode capacity degrades noticeably as the silicon region is cycled[64]. For comparison, the positive electrode is more degraded (lower y-axis values), but is unaffected by the DoD. **f**, Positive electrode capacity versus rest fraction at high SOC. **g**, Example of curve fitting for Q_{Li} versus EFC up to 90% SOH. **h**, Fitting errors for all cells across all C-rates.

several features playing a similarly important role. Finally, the lithium inventory (Q_{Li}) also exhibits more complex dependencies on dynamic discharge features, although the dominant features for both Q_{pe} and Q_{ne}, namely, the rest fraction at high state of charge (SOC) and the current variance, appear to be important.

The variability in cycle life at 90% SOH (Fig. 3b and Fig. 4a) can thus be explained by the maximum instantaneous discharge currents and the rest fraction at high SOC. On the one hand, the role of current peaks can be explained by their importance on negative electrode capacity and resistance build-up (Fig. 3c). On the other hand, the rest fraction at high SOC is mostly detrimental to the positive electrode.

Moreover, the impact of the degradation modes evolves as the cells age. Figure 4a,b illustrates that the degradation is initially dominated by the loss of lithium inventory (Q_{Li}). This corresponds to side reactions beyond the intercalation reaction, happening at the beginning of battery life, such as solid electrolyte interphase growth. The Q_{Li} degradation trajectory is well described by the fitting equation $1 + a \times EFC^{0.5} + b \times EFC$, with Fig. 4g,h showing a mean absolute percentage error (MAPE) of less than 0.5%.

However, as the batteries age, additional degradation mechanisms become important. On the one hand, the positive electrode capacity loss dominates and is impacted by the rest fraction at high SOC (Fig. 4f,

Supplementary Fig. 10 and Supplementary Notes), consistent with the instability of positive electrodes at higher voltages[62,63]. Supplementary Figs. 11 and 12 confirm that for both constant current protocols and highway protocols with rests, the capacity degradation accelerates when the rest is at a higher SOC. On the other hand, the negative electrode capacity loss (which is less than the positive electrode capacity loss) is impacted by the DoD (Fig. 4c–e). Large instantaneous discharge current and variance give rise to larger overpotentials, as already mentioned. Consequently, the lower cut-off voltage is reached earlier, decreasing the DoD and thus preventing cycling at very low SOC. In this low SOC region, silicon is electrochemically active and is known to degrade faster[64]. Figure 4d shows that, in particular at low average C-rates, when the DoD is beyond 85%, the negative electrode capacity degrades more rapidly, while cells avoiding deep discharge have more preserved negative electrode capacities, in agreement with Fig. 3e. In addition, the DoD has no impact on the positive electrode capacity (Fig. 4e). We emphasize that Q_{ne} degrades less than Q_{pe} (Fig. 4d,e), contributing to the battery lifetime being dominated by Q_{pe} degradation, as emphasized in Fig. 4a. Although these results provide insights on degradation modes, future studies to evaluate the impact of dynamic cycling at the material level are needed to deepen our understanding of the degradation mechanisms.

Conclusions

We have pinpointed strong correlations between dynamic discharge profiles and battery ageing under non-accelerated conditions. We found that constant current is not representative of ageing under real EV driving and dynamic cycling enhances battery lifetime. In addition, time-induced ageing becomes dominant over cycling ageing, even at EV-relevant C-rates (≤0.4C). Furthermore, leveraging the diversity of our dynamic discharge profiles, we evidenced that low-frequency pulses, discharge current peaks and time-induced ageing, all characteristic of real EV usage behaviour, play a decisive role in degradation trajectories.

This work shows that cycling experiments need to be carried out with realistic loads to capture degradation trends. The present dataset can be used to develop models to map degradation induced by constant current to degradation induced by dynamic cycling. There is a need to systematically adopt realistic cycling protocols when developing new battery materials and cell designs, not only in terms of optimization but also in terms of mechanistic understanding. Beyond battery research, this work illustrates the opportunities to use realistic testing to deepen our understanding of material and device ageing in physical sciences.

Methods

Ageing experiments

Ninety-two commercial EV energy lithium-ion cells (silicon oxide–graphite/nickel cobalt aluminium) were cycled using a Maccor Series 4000 battery cycler with four-point contact cylindrical cell fixtures (Korea Thermo-Tech and SpectraPower). The batteries were held at a constant temperature of 35 °C inside a CSZ temperature chamber (model ZPS-16-2-H/AC; Supplementary Fig. 13). The experiments were conducted in the SLAC-Stanford Battery Center for over 2 years. The data acquisition and management set-up is described in Supplementary Method 2. We encountered two cell failures, but each of the 47 protocols described hereafter was duplicated (Supplementary Table 4). These protocols were designed on the basis of continuous-use EV applications (autonomous and non-autonomous) such as buses, taxis, commercial or industrial vehicles. Depending on battery pack sizing and applications, daily usage of 10 h or longer could be expected. As a result, the cells were continuously discharged until reaching the cut-off limit. Most of the discharge profiles did not include important rest periods, commonly found in consumer-driven EV profiles[65]. Of the four protocol types (Fig. 1), real driving cycles were the most realistic of EV driving, followed by the synthetic, periodic and constant current protocols in this order. We charged all the cells using the same constant current–constant voltage protocol (C/2 to 4.2 V, 0.05C cut-off).

Constant current protocols

To provide a baseline reference for the dynamic profiles, we incorporated constant current protocols into the experiment design. Within the constant current protocols, we tested four different discharge profiles, one consisting of a simple discharge and three others that included a storage period (rest) of 6 h at 5%, 50% or 100% SOC before completing the discharge (Fig. 1). The 6 h duration was a design choice to capture rest periods before, during or after discharge. These intermediate SOC values are defined by voltages, extracted from an open-circuit voltage curve obtained using a galvanostatic intermittent titration technique.

The aim was to concretely identify the effect of the SOC at rest on ageing when combined with cycling (rests at higher SOC are known to accelerate degradation in the context of calendar ageing[8,66]). This also emulates three different driving behaviours, depending on when users charge their vehicle. The current profiles of these protocols are shown in Supplementary Fig. 14 for a C/10 discharge current.

Periodic protocols

We define the first type of dynamic discharge protocols as 'periodic protocols'. These consisted of a discharge pulse followed by a short charge pulse, intended to simulate a driving discharge segment, followed by a regenerative braking charging segment, followed by a rest. The periodic protocols were designed to represent a specific aspect of a driving trip, for which we varied different parameters, such as the charge/discharge ratio, frequency and relative braking magnitude, and included a superposition of two signals.

A schematic representation of the structure of the periodic profiles for a single sequence is shown in Supplementary Fig. 15. For all periodic profiles, this sequence was repeated until the battery went from fully charged to the lower cut-off voltage (3.1 V). Five different periodic profiles were generated by varying the parametrization of the periodic sequence. See Supplementary Method 3 and Supplementary Tables 5 and 6 for more details. A single periodic sequence and a full discharge are shown in Supplementary Fig. 16 for all of the periodic profiles (plotted at an average C-rate of C/10).

Drive protocols

Real driving protocols were also tested. These contained driving data from two different cities (referred to as City 1 and City 2). They were also used to generate the synthetic profiles (see below). The two driving profiles were cycled at average C-rates of C/10 and C/16, which was achieved by properly scaling the current to the desired average C-rate. The driving profiles cycled at C/10 reached the lower cut-off voltage (3.1 V), while the two C/16 driving profiles (four cells) did not; these latter profiles were excluded from subsequent analyses but kept in the dataset for completeness. The profiles for the C/10 average C-rate case are plotted in Supplementary Fig. 17.

Synthetic protocols

Synthetic discharge protocols were designed to emulate trips between a start and end location. We tested several different synthetic profiles that captured highway driving, urban driving and a combination of the two, based on driving data from two cities. Synthetic profile 1a contained a single highway trip from City 1 followed by a rest. Synthetic profile 1b contained four consecutive highway trips from City 1 followed by a longer rest. Profiles 2a and 2b contained characteristic urban driving trips from City 1 and City 2, respectively. Synthetic profile 2c contained a characteristic urban driving trip from the driving profiles of City 1 and City 2 combined. Finally, synthetic profile 3 captured mixed urban and highway driving obtained by concatenating profiles 2a, 2b, 2c and 1a. These synthetic profiles were generated from the real city driving data from City 1 and City 2 using an algorithm previously developed by Moy et al.[67] (for details, see ref. 41).

Highway-based duty cycles 1a and 1b (C/2 average) were excluded because the instantaneous current exceeded hardware limits and were replaced by a C/16 average protocol. Synthetic duty cycle 3 (C/2 average) was also excluded for the same reason.

As for the periodic profiles, all of the synthetic profiles were repeated until the batteries went from fully charged to the discharge cut-off voltage (3.1 V). A single sequence and a full discharge are shown in Supplementary Fig. 18 for each of the synthetic profiles (plotted at C/10 average C-rate).

Diagnostic cycles

To assess the extent of degradation induced by the ageing cycles, we applied standardized diagnostic cycles conducted periodically during the cycling experiments to probe the state of the batteries, as commonly reported in the literature[8,68–70]. Diagnostic cycles were run at cycle 0 (before any ageing cycles), then after 25, 50, 75 and 100 ageing cycles to provide higher granularity in diagnostic metric trajectories in the early degradation cycles and then after every 100 cycles.

The full diagnostic cycle applied to the batteries is shown in Supplementary Fig. 19. A C/3 reset cycle removed the effects from the previous ageing cycle. A voltage-based pulse routine (Supplementary Fig. 20) and an HPPC routine (Supplementary Fig. 21), separated by

another C/3 reset cycle, were then carried out to extract discharge resistance metrics (Ohmic resistance ($R_{0.03s}$), charge-transfer resistance (R_{3s}) and polarization resistance (R_{10s}) were calculated using equation (1), as illustrated in Supplementary Fig. 22, where OCV is the open-circuit voltage before the pulse is applied, and I_2 is the applied pulse current). Note that, due to data acquisition limitations, the Ohmic resistance was calculated 0.03 s after the start of the pulse, hence the term $R_{0.03s}$. Finally, a C/40 and C/2 RPT were performed[71]. The protocols included in the diagnostic cycle (such as the RPTs) used a voltage range of 2.8–4.2 V. Further details on each diagnostic sequence are included in Supplementary Method 4.

$$R_{x\,\text{seconds}} = \frac{V_{x\,\text{seconds after pulse}} - \text{OCV}}{I_o} \tag{1}$$

EoL was defined as 85% SOH, using the discharge capacity data from the C/2 RPT to capture degradation due to both thermodynamic and kinetic effects. Non-monotonically decreasing capacity data points were ignored to ensure reliable EoL criteria. EFCs were obtained using equation (2).

$$\text{EFC} = \frac{\text{Total capacity throughput (including diagnostic cycles)}}{2 \times \text{Nominal capacity}} \tag{2}$$

Fitting the SOH degradation curves with a simple linear model was insufficient and adding the $X^{0.5}$ dependence was critical to obtain good results, as discussed in Supplementary Method 5 and Supplementary Figs. 23 and 24.

We used the diagnostic cycle C/40 RPT to estimate the capacities of the positive electrode (Q_{pe}), negative electrode (Q_{ne}) and lithium inventory (Q_{Li}) using a mechanistic fitting method based on the work of Dubarry and co-workers[52–54]. This approach has also been applied by Birkl et al.[72], who experimentally confirmed the validity of this approach (for further details, see Supplementary Method 6 and Supplementary Figs. 25–28).

ML architecture

To understand why these different ageing profiles induce different degradation behaviours, we deployed an interpretable ML pipeline that included featurizing the ageing cycles, training XGBoost models and running SHAP analyses.

First, we parametrized the discharge profiles. We processed data from a single ageing cycle representative of the long-term cycling experiments using time-series current data only. We extracted a total of 12 parameters that could be related to real vehicle operation, such as the average C-rate, the current variance (normalized) or the charge/discharge ratio. In addition, the current signal was Fourier transformed to recover the key peak frequencies in each discharge protocol. Supplementary Method 7 provides more details about this featurization procedure and Supplementary Table 3 lists all features generated. For robustness and repeatability of our ML pipeline, we removed correlated features, as discussed in Supplementary Method 7 and Supplementary Fig. 29.

Due to the high dimensionality of the operating conditions space (input), relationships with EoL metrics (outputs) were not obvious. To deconvolute the impacts of individual protocol parameters, we applied explainable ML models. We used the discharge profile parameters as input features in an XGBoost ML model[73] (using XGBRegressor in XGBoost with a wrapper from the scikit-learn library[74]) to predict selected target outputs. The XGBoost model was chosen for its high performance and flexibility. Its parameters are detailed in Supplementary Table 7. The outputs calculated for this analysis were EFCs, Q_{pe}, Q_{ne}, Q_{Li}, $R_{0.03s}$, R_{3s} and R_{10s} at EoL (degradation modes). The resistances were extracted from the HPPCs at 50% SOC during the discharge pulse. Predictions are shown in Supplementary Figs. 30 and 31.

We used SHAP analysis to calculate feature importance[70,75]. Comparing SHAP values gives a statistical quantification of the importance of each discharge profile feature. Despite removing highly correlated features, SHAP results still exhibited some dependence on the random seed. To address this issue, the average of 25 random seed runs is reported. The results were consistent across repeats (Supplementary Fig. 32) and different train–test splits (Supplementary Fig. 33). The variability in the EoL metrics is dependent on both the variability induced by the average C-rate (as illustrated in Fig. 2d) and the variability induced by protocol-specific characteristics. In this work, we were interested in explaining the variability not induced by the average C-rate. As a result, Fig. 3 represents the SHAP values for all features except the average C-rate. The same strategy was used in Fig. 4a,b to remove C-rate dependencies.

Data availability

The battery dataset is available via Stanford Digital Repository at https://purl.stanford.edu/td676xr4322. The data needed to replicate the analyses and figures are available on Github at https://github.com/geslina. Source data are provided with this paper.

Code availability

The code needed to replicate the analyses and figures is available on Github at https://github.com/geslina.

References

1. Hu, X., Xu, L., Lin, X. & Pecht, M. Battery lifetime prognostics. *Joule* **4**, 310–346 (2020).
2. Saha, B. & Goebel, K. *Battery Data Set* (NASA Prognostics Data Repository, 2007).
3. dos Reis, G., Strange, C., Yadav, M. & Li, S. Lithium-ion battery data and where to find it. *Energy AI* **5**, 100081 (2021).
4. Zhu, J. et al. Data-driven capacity estimation of commercial lithium-ion batteries from voltage relaxation. *Nat. Commun.* **13**, 2261 (2022).
5. He, W., Williard, N., Osterman, M. & Pecht, M. Prognostics of lithium-ion batteries based on Dempster–Shafer theory and the Bayesian Monte Carlo method. *J. Power Sources* **196**, 10314–10321 (2011).
6. Diao, W., Saxena, S. & Pecht, M. Accelerated cycle life testing and capacity degradation modeling of LiCoO$_2$-graphite cells. *J. Power Sources* **435**, 226830 (2019).
7. Paulson, N. H. et al. Feature engineering for machine learning enabled early prediction of battery lifetime. *J. Power Sources* **527**, 231127 (2022).
8. Wildfeuer, L. et al. Experimental degradation study of a commercial lithium-ion battery. *J. Power Sources* **560**, 232498 (2023).
9. Devie, A., Baure, G. & Dubarry, M. Intrinsic variability in the degradation of a batch of commercial 18650 lithium-ion cells. *Energies* **11**, 1031 (2018).
10. Preger, Y. et al. Degradation of commercial lithium-ion cells as a function of chemistry and cycling conditions. *J. Electrochem. Soc.* **167**, 120532 (2020).
11. Nuhic, A., Terzimehic, T., Soczka-Guth, T., Buchholz, M. & Dietmayer, K. Health diagnosis and remaining useful life prognostics of lithium-ion batteries using data-driven methods. *J. Power Sources* **239**, 680–688 (2013).
12. Jossen, A. Fundamentals of battery dynamics. *J. Power Sources* **154**, 530–538 (2006).
13. Pozzato, G. et al. Analysis and key findings from real-world electric vehicle field data. *Joule* **7**, 2035–2053 (2023).
14. Liu, Z., Onori, S. & Ivanco, A. Synthesis and experimental validation of battery aging test profiles based on real-world duty cycles for 48-V mild hybrid vehicles. *IEEE Trans. Veh. Technol.* **66**, 8702–8709 (2017).

15. Naumann, M., Spingler, F. B. & Jossen, A. Analysis and modeling of cycle aging of a commercial LiFePO$_4$/graphite cell. *J. Power Sources* **451**, 227666 (2020).

16. Schmalstieg, J., Käbitz, S., Ecker, M. & Sauer, D. U. A holistic aging model for Li(NiMnCo)O$_2$ based 18650 lithium-ion batteries. *J. Power Sources* **257**, 325–334 (2014).

17. Liu, Z., Ivanco, A. & Onori, S. Aging characterization and modeling of nickel-manganese-cobalt lithium-ion batteries for 48V mild hybrid electric vehicle applications. *J. Energy Storage* **21**, 519–527 (2019).

18. Sarasketa-Zabala, E., Gandiaga, I., Martinez-Laserna, E., Rodriguez-Martinez, L. & Villarreal, I. Cycle ageing analysis of a LiFePO$_4$/graphite cell with dynamic model validations: towards realistic lifetime predictions. *J. Power Sources* **275**, 573–587 (2015).

19. Sarasketa-Zabala, E. et al. Realistic lifetime prediction approach for Li-ion batteries. *Appl. Energy* **162**, 839–852 (2016).

20. Baure, G. & Dubarry, M. Synthetic vs. real driving cycles: a comparison of electric vehicle battery degradation. *Batteries* **5**, 42 (2019).

21. Lorenzo, C., Tabusse, R., Bouquain, D., Hibon, S. & Hissel, D. Study of lithium-ion battery ageing cycled with current profiles from railway applications. In *2021 IEEE Vehicle Power and Propulsion Conference (VPPC)* 1–6 (IEEE, 2021).

22. Peterson, S. B., Apt, J. & Whitacre, J. Lithium-ion battery cell degradation resulting from realistic vehicle and vehicle-to-grid utilization. *J. Power Sources* **195**, 2385–2392 (2010).

23. Keil, P. & Jossen, A. Impact of dynamic driving loads and regenerative braking on the aging of lithium-ion batteries in electric vehicles. *J. Electrochem. Soc.* **164**, A3081–A3092 (2017).

24. Carrilero, I. et al. Impact of fast-charging and regenerative braking in LiFePO$_4$ batteries for electric bus applications. In *2017 IEEE Vehicle Power and Propulsion Conference (VPPC)* 1–6 (IEEE, 2017).

25. Pozzato, G., Allam, A. & Onori, S. Lithium-ion battery aging dataset based on electric vehicle real-driving profiles. *Data Brief* **41**, 107995 (2022).

26. Dynamometer drive schedules. *EPA* https://www.epa.gov/vehicle-and-fuel-emissions-testing/dynamometer-drive-schedules (2022).

27. Castillo, E. C. Standards for electric vehicle batteries and associated testing procedures. In *Advances in Battery Technologies for Electric Vehicles* 469–494 (Woodhead Publishing, 2015).

28. *Electric Vehicle Battery Test Procedures Manual Revision 2* (USABC/DOE, 1996); http://avt.inl.gov/sites/default/files/pdf/battery/usabc_manual_rev2.pdf

29. Uno, M. & Tanaka, K. Influence of high-frequency charge–discharge cycling induced by cell voltage equalizers on the life performance of lithium-ion cells. *IEEE Trans. Veh. Technol.* **60**, 1505–1515 (2011).

30. Uddin, K., Moore, A. D., Barai, A. & Marco, J. The effects of high frequency current ripple on electric vehicle battery performance. *Appl. Energy* **178**, 142–154 (2016).

31. Chang, F., Roemer, F. & Lienkamp, M. Influence of current ripples in cascaded multilevel topologies on the aging of lithium batteries. *IEEE Trans. Power Electron.* **35**, 11879–11890 (2020).

32. Amamra, S.-A., Tripathy, Y., Barai, A., Moore, A. D. & Marco, J. Electric vehicle battery performance investigation based on real world current harmonics. *Energies* **13**, 489 (2020).

33. Bessman, A., Soares, R., Wallmark, O., Svens, P. & Lindbergh, G. Aging effects of AC harmonics on lithium-ion cells. *J. Energy Storage* **21**, 741–749 (2019).

34. Juang, L. W. et al. Investigation of the influence of superimposed AC current on lithium-ion battery aging using statistical design of experiments. *J. Energy Storage* **11**, 93–103 (2017).

35. Beh, H. Z. Z., Covic, G. A. & Boys, J. T. Effects of pulse and DC charging on lithium iron phosphate (LiFePO$_4$) batteries. In *2013 IEEE Energy Conversion Congress and Exposition* 315–320 (IEEE, 2013).

36. Ferraz, P. K. P. & Kowal, J. A comparative study on the influence of DC/DC-converter induced high frequency current ripple on lithium-ion batteries. *Sustainability* **11**, 6050 (2019).

37. Breucker, S. D., Engelen, K., D'hulst, R. & Driesen, J. Impact of current ripple on Li-ion battery ageing. In *2013 World Electric Vehicle Symposium and Exhibition (EVS27)* 1–9 (IEEE, 2013).

38. Steinstraeter, M., Gandlgruber, J., Everken, J. & Lienkamp, M. Influence of pulse width modulated auxiliary consumers on battery aging in electric vehicles. *J. Energy Storage* **48**, 104009 (2022).

39. Brand, M. J., Hofmann, M. H., Schuster, S. S., Keil, P. & Jossen, A. The influence of current ripples on the lifetime of lithium-ion batteries. *IEEE Trans. Veh. Technol.* **67**, 10438–10445 (2018).

40. Ghassemi, A., Hollenkamp, A. F., Banerjee, P. C. & Bahrani, B. Impact of high-amplitude alternating current on LiFePO$_4$ battery life performance: investigation of AC-preheating and microcycling effects. *Appl. Energy* **314**, 118940 (2022).

41. Moy, K., Ganapathi, D., Geslin, A., Chueh, W. & Onori, S. Synthetic duty cycles from real-world autonomous electric vehicle driving. *Cell Rep. Phys. Sci.* **4**, 101536 (2023).

42. Frenander, K. & Thiringer, T. Low frequency influence on degradation of commercial Li-ion battery. *Electrochim. Acta* **462**, 142760 (2023).

43. Qin, Y. et al. A rapid lithium-ion battery heating method based on bidirectional pulsed current: heating effect and impact on battery life. *Appl. Energy* **280**, 115957 (2020).

44. Ecker, M. et al. Development of a lifetime prediction model for lithium-ion batteries based on extended accelerated aging test data. *J. Power Sources* **215**, 248–257 (2012).

45. Ecker, M. et al. Calendar and cycle life study of Li(NiMnCo)O$_2$-based 18650 lithium-ion batteries. *J. Power Sources* **248**, 839–851 (2014).

46. Schimpe, M. et al. Comprehensive modeling of temperature-dependent degradation mechanisms in lithium iron phosphate batteries. *J. Electrochem. Soc.* **165**, A181 (2018).

47. Naumann, M., Schimpe, M., Keil, P., Hesse, H. C. & Jossen, A. Analysis and modeling of calendar aging of a commercial LiFePO$_4$/graphite cell. *J. Energy Storage* **17**, 153–169 (2018).

48. Keil, P. & Jossen, A. Calendar aging of NCA lithium-ion batteries investigated by differential voltage analysis and Coulomb tracking. *J. Electrochem. Soc.* **164**, A6066–A6074 (2016).

49. Smith, A. J., Dahn, H. M., Burns, J. C. & Dahn, J. R. Long-term low-rate cycling of LiCoO$_2$/graphite Li-ion cells at 55 °C. *J. Electrochem. Soc.* **159**, A705 (2012).

50. Developing infrastructure to charge electric vehicles. *US Department of Energy* https://afdc.energy.gov/fuels/electricity-infrastructure.html

51. Pesaran, A., Santhanagopalan, S. & Kim, G.-H. Addressing the impact of temperature extremes on large format Li-ion batteries for vehicle applications. In *Proc. 30th International Battery Seminar* (Department of Energy at National Renewable Energy Lab, 2013).

52. Dubarry, M., Truchot, C. & Liaw, B. Y. Synthesize battery degradation modes via a diagnostic and prognostic model. *J. Power Sources* **219**, 204–216 (2012).

53. Dubarry, M. & Beck, D. Big data training data for artificial intelligence-based Li-ion diagnosis and prognosis. *J. Power Sources* **479**, 228806 (2020).

54. Dubarry, M. & Beck, D. Perspective on mechanistic modeling of Li-Ion batteries. *Acc. Mater. Res.* **3**, 843–853 (2022).

55. Zhao, J., Gao, Y., Guo, J., Chu, L. & Burke, A. F. Cycle life testing of lithium batteries: the effect of load-leveling. *Int. J. Electrochem. Sci.* **13**, 1773–1786 (2018).

56. Geslin, A. et al. Selecting the appropriate features in battery lifetime predictions. *Joule* **7**, 1956–1965 (2023).

57. Jin, N. *Morphological Control and Multi-Length-Scale Characterization of Lithium-Iron Phosphate*. PhD thesis, Stanford Univ. (2022).

58. Deng, H. D. *The Electrochemical Phase Transformation in Li$_x$FePO$_4$*. PhD thesis, Stanford Univ. (2021).

59. Deng, H. D. et al. Beyond constant current: origin of pulse-induced activation in phase-transforming battery electrodes. *ACS Nano* **18**, 2210–2218 (2024).

60. Aiken, C. P. et al. Tracking electrolyte motion in cylindrical Li-ion cells using moment of inertia measurements. *J. Electrochem. Soc.* **170**, 040529 (2023).

61. Guo, J. et al. Unravelling the mechanism of pulse current charging for enhancing the stability of commercial LiNi$_{0.5}$Mn$_{0.3}$Co$_{0.2}$O$_2$/graphite lithium-ion batteries. *Adv. Energy Mater.* **14**, 2400190 (2024).

62. Gent, W. E., Busse, G. M. & House, K. Z. The predicted persistence of cobalt in lithium-ion batteries. *Nat. Energy* **7**, 1132–1143 (2022).

63. Li, W., Asl, H. Y., Xie, Q. & Manthiram, A. Collapse of LiNi$_{1-x-y}$Co$_x$Mn$_y$O$_2$ lattice at deep charge irrespective of nickel content in lithium-ion batteries. *J. Am. Chem. Soc.* **141**, 5097–5101 (2019).

64. Kirkaldy, N., Samieian, M. A., Offer, G. J., Marinescu, M. & Patel, Y. Lithium-ion battery degradation: measuring rapid loss of active silicon in silicon–graphite composite electrodes. *ACS Appl. Energy Mater.* **5**, 13367–13376 (2022).

65. Dubarry, M., Baure, G. & Devie, A. Durability and reliability of EV batteries under electric utility grid operations: path dependence of battery degradation. *J. Electrochem. Soc.* **165**, A773 (2018).

66. Keil, P. et al. Calendar aging of lithium-ion batteries. *J. Electrochem. Soc.* **163**, A1872 (2016).

67. Moy, K., Lee, S. B., Harris, S. & Onori, S. Design and validation of synthetic duty cycles for grid energy storage dispatch using lithium-ion batteries. *Adv. Appl. Energy* **4**, 100065 (2021).

68. Weng, A. et al. Predicting the impact of formation protocols on battery lifetime immediately after manufacturing. *Joule* **5**, 2971–2992 (2021).

69. Eldesoky, A. et al. Long-term study on the impact of depth of discharge, C-rate, voltage, and temperature on the lifetime of single-crystal NMC811/artificial graphite pouch cells. *J. Electrochem. Soc.* **169**, 100531 (2022).

70. van Vlijmen, B. et al. Interpretable data-driven modeling reveals complexity of battery aging. Preprint at https://doi.org/10.26434/chemrxiv-2023-zdl2n (2023).

71. Christophersen, J. P. *Battery Technology Life Verification Test Manual Revision 1* (US Department of Energy, 2012).

72. Birkl, C. R., Roberts, M. R., McTurk, E., Bruce, P. G. & Howey, D. A. Degradation diagnostics for lithium ion cells. *J. Power Sources* **341**, 373–386 (2017).

73. Chen, T. & Guestrin, C. XGBoost: a scalable tree boosting system. In *Proc. 22nd ACM SIGKDD International Conference on Knowledge Discovery and Data Mining* 785–794 (ACM, 2016).

74. Pedregosa, F. et al. Scikit-learn: machine learning in Python. *J. Mach. Learn. Res.* **12**, 2825–2830 (2011).

75. Lundberg, S. M. & Lee, S.-I. in *Advances in Neural Information Processing Systems* Vol. 30 (eds Guyon, I. et al.) 4768–4777 (Curran Associates, 2017).

Acknowledgements

Author contributions

A.G.: conceptualization, methodology, software, data curation and analysis, visualization, writing—original draft, review and editing, project administration. L.X.: methodology, data curation and analysis, software, visualization, writing—review and editing, project administration. D.G.: conceptualization, initial software development, initial data curation and analysis, visualization, writing—original draft, review and editing, project administration. K.M.: conceptualization, writing—review and editing. W.C.C.: conceptualization, resources, writing—review and editing, supervision, funding acquisition. S.O.: conceptualization, writing—review and editing, supervision, funding acquisition.

Competing interests

The authors declare no competing interests.

Additional information

Supplementary information The online version contains supplementary material available at https://doi.org/10.1038/s41560-024-01675-8.

Correspondence and requests for materials should be addressed to William C. Chueh or Simona Onori.

Peer review information *Nature Energy* thanks Evelina Wikner, Jiangong Zhu and the other, anonymous, reviewer(s) for their contribution to the peer review of this work.

Reprints and permissions information is available at www.nature.com/reprints.

Publisher's note Springer Nature remains neutral with regard to jurisdictional claims in published maps and institutional affiliations.